Dust Properties of Clumpy Disc Galaxies at $z\sim1.3$ with Herschel-SPIRE*

Emily Wisnioski^{1,2}†, Karl Glazebrook², Chris Blake², Mark Swinbank³

- ¹ Max-Planck-Institut für extraterrestrische Physik, Postfach 1312, Giessenbachstr., D-85741 Garching, Germany.
- ² Centre for Astrophysics and Supercomputing, Swinburne University of Technology, P.O. Box 218, Hawthorn, VIC 3122, Australia.
- ³Institute for Computational Cosmology, Durham University, South Road, Durham DH1 3LE, UK.

Accepted 2013 August 17. Received 2013 August 16; in original form 2013 July 10

ABSTRACT

We present the far-infrared derived dust properties from Herschel SPIRE of the WiggleZ kinematic sample of 13 star-forming galaxies at $z \sim 1.3$, with existing ancillary \sim kpc resolution integral field spectroscopy. We detect 3 galaxies individually and place limits on the remainder by stacking. The detected galaxies, two clumpy discs and one merger, have cold dust temperatures of $T_{\rm d} \sim 26~{\rm K}$ and have infrared luminosities of $L_{\rm IR} \sim 1.2 \times 10^{12}~{\rm L}_{\odot}$, determined by modified blackbody fitting. The two detected disc galaxies have the largest $H\alpha$ surface areas of the sample and have the reddest ultraviolet to near-infrared spectral energy distributions. The likely source of the infrared luminosity in these objects is dust heated by the interstellar radiation field and young stellar emission from the clumps within the discs. The source of infrared luminosity for the merger is likely a dust heated by a starburst resulting from the merger. The WiggleZ detections are among the coldest and lowest luminosity individual objects detected in the far-infrared at z > 1. When combining the kinematic data, we find that none of the compact galaxies nor the 'dispersion dominated' galaxies of the WiggleZ kinematic sample are detected, implying that they have warmer dust temperatures. The compact objects show the highest $H\alpha$ velocity dispersions in the sample, in qualitative agreement with bulge formation models. These far-infrared results strengthen the interpretation that the majority of galaxies in this sample constitute different stages in clumpy disc formation as presented from ancillary kinematic analysis.

Key words: galaxies: kinematics and dynamics – galaxies: formation – galaxies: evolution – infrared: galaxies

1 INTRODUCTION

The majority of results from $z\sim 1$ galaxy formation studies have utilised observations of the rest-frame optical where key physical and chemical parameters can be measured from nebular emission lines, e.g. star formation rates (SFRs) and metallicity (from H α , H β , [NII], [OII], [OIII]). However, these lines can be strongly attenuated by intervening dust within galaxies. Locally, where high spatial resolution studies of dusty galaxies has been possible, prescriptions to account for the global effects of dust have been calibrated. For studies of star-forming galaxies at z>1 estimates of dust extinction are either determined using calibrations set from lo-

† E-mail: emily@mpe.mpg.de

cal analogs or spectral fits to broad-band photometry. However, both methods are highly uncertain as in the first case there the local relations may not hold for the early universe (Kennicutt et al. 2009) and in the later case estimates can be severely limited by degeneracies between dust extinction and age (e.g. Gordon et al. 1997). Accurate dust corrections at high-redshift will be especially important for upcoming galaxy surveys from new near-infrared instruments that will rely on H α for SFR estimates. Furthermore, it has been suggested that star-forming galaxies (SFGs) were dustier in the past (e.g. Takeuchi et al. 2005) which if not well understood could lead to misinterpretation of the true evolution in galaxy properties.

The launch of modern far-infrared (FIR) facilities, including the *Herschel Space Observatory* (Pilbratt et al. 2010), has made it possible to directly investigate dust properties of star-forming galaxies from $z \sim 0-3$. With past

^{*} Herschel is an ESA space observatory with science instruments provided by European-led Principal Investigator consortia and with important participation from NASA.

facilities only the brightest objects were detectable, making it difficult to study dust in a representative sample of star-forming galaxies at high redshift. The galaxies studied were typically classified as mergers, starburst galaxies or submillimeter galaxies (e.g. Soifer et al. 2008) that lie above the main locus of galaxies in the SFR-stellar mass plane (Daddi et al. 2007). Herschel has allowed the first direct detections of more representative star-forming, or 'main sequence', galaxies at $z \gtrsim 1$ (e.g. Elbaz et al. 2011; Burgarella et al. 2011; Roseboom et al. 2012; Magnelli et al. 2012b; Oteo et al. 2013). Measurements of dust extinction in high redshift galaxies are made from these observations by studying the relationship between infrared SFRs and $H\alpha$ SFRs. A comparison of the ratio of these two SFR indicators with additional methods of measuring dust extinction yield a good agreement between methods using ~500 galaxies at z = 0.06 - 0.46, covering a wide range of masses and SFRs (Domínguez et al. 2012), and ~ 60 far-infrared selected sources at $z \sim 1$ of star-forming galaxies (Roseboom et al. 2012), suggesting that local calibrations are appropriate to use for high redshift galaxies. However, at both redshifts a correlation is seen between metallicity and the ratio of infrared to $H\alpha$ SFRs that may be redshift dependent.

Results from studies locally and at high redshift, where ancillary data is available, indicate a correlation between infrared luminosities and morphology and/or galaxy type (e.g. Sanders et al. 1988; Sanders & Mirabel 1996; Ishida 2004; Kartaltepe et al. 2010b, 2011). Statistical results from z = 0.1 - 3.5 suggest that $L_{\rm IR} \sim 5 \times 10^{11} \ {\rm L_{\odot}}$ is the quantitative dividing luminosity between the dominance of spirals and major mergers, comparable to current detection limits of Herschel at $z \sim 1$ (Kartaltepe et al. 2011). Thus, despite the higher sensitivity of the new space-based facilities compared to ground-based facilities, observations of large samples of star-forming galaxies (SFGs) at $z \gtrsim 1$ have remained a challenge. Long integrations are needed, severely limiting large surveys of this population and confining searches for high-redshift detections to the Hubble deep fields. Stacking is still often required to derive infrared properties of UVselected galaxies at z > 1 (Magdis et al. 2010; Reddy et al. 2012; Ibar et al. 2013).

Dust temperatures derived from far infrared photometry have also been shown to correspond on average with morphology and galaxy type (Elbaz et al. 2011; Magnelli et al. 2012b). Star-forming galaxies at 0 < z < 2.5 have cooler effective dust temperatures ($\sim 31~\rm K$) than starburst galaxies or submillimeter galaxies (SMGs; $\sim 40~\rm K$; Elbaz et al. 2011; Magnelli et al. 2012b). Galaxies with hot dust temperatures tend to be more compact (Elbaz et al. 2011) and have disturbed morphologies indicative of major mergers, while galaxies with cold dust temperatures have disc-like morphologies (Magnelli et al. 2012b). However, even with deep space-based imaging, at z > 1 morphologies are hard to classify kinematically due to the high number of irregular galaxies which confuse the simple disc vs. merger classification.

This paper presents far-infrared observations of 13 galaxies with ancillary ${\rm H}\alpha$ kinematics from integral field spectroscopy in order to directly compare dust properties with global galaxy motions. The observations and derivation of fluxes from Herschel/SPIRE for the WiggleZ kinematic sample are described in Section 2. Modified blackbody fits

are applied in Section 3 to estimate total infrared luminosities, dust temperatures, and dust masses. The dust extinction derived from the ratio of $H\alpha$ and infrared luminosities is compared to that derived from SED fitting to ultraviolet (UV) to near-infrared (NIR) photometry. Section 4 looks at the correlation between kinematic properties and dust properties, re-evaluating the galaxy classifications made in Wisnioski et al. (2011). A standard Λ CDM cosmology of $\Omega_{\rm m}=0.27,~\Omega_{\Lambda}=0.73,~h=0.71$ is adopted throughout this paper with a Baldry-Glazebrook initial mass function (IMF; BG03; Baldry & Glazebrook 2003). In this cosmology, at redshift z=1.3,1 arcsec corresponds to 8.44 kpc.

2 OBSERVATIONS AND DATA

We present FIR observations for 13 UV-selected galaxies at $z \sim 1.3$ selected from the WiggleZ Dark Energy Survey (Drinkwater et al. 2010) and observed using integral field spectroscopy (IFS) with the OSIRIS instrument on the Keck telescopes (Wisnioski et al. 2011). The galaxies in this sample are ideal targets for *Herschel* because they are among the most luminous UV-selected sources at $z \sim 1.3$. They were originally selected as being possible starbursts due to ULIRG-like star formation rates measured from their optical spectra (Wisnioski et al. 2011). A fraction of the sample (7/13) have subsequently been found to be more disclike, representing the luminous end of main-sequence starforming galaxies with $SFR_{H\alpha} \sim 40 M_{\odot} \text{ yr}^{-1}$. Thus, although the sample is UV-selected, suggesting low dust extinction, the high H α luminosities (more typical of $z \sim 2$ galaxies) indicate that these objects are detectable by Herschel if $A_V \sim 1$, normally assumed for emission line studies of SFGs (e.g. Kennicutt 1992; Tresse et al. 1996) and inline with estimates from their spectral energy distributions (SEDs). Furthermore, 5/13 of the galaxies appear to be compact similar to SMGs with chaotic kinematics possibly representing the strong starbursts resulting from major mergers (e.g. Swinbank et al. 2008; Engel et al. 2010). Finally, at $z \sim 1.3$ the three Herschel bands at 250, 350, and 500 μm would straddle the peak of the infrared SED allowing constraints on the dust temperature.

2.1 OSIRIS sample

The ${\rm H}\alpha$ morphological classifications defined in Wisnioski et al. (2011) are discussed here in the context of the Herschel observations. In brief, the sample can be broken down into three morphological classes based on their ${\rm H}\alpha$ images; 'single emission galaxies' appear as resolved compact galaxies, 'extended emission galaxies' typically have a bright knot of emission with tails or accompanying diffuse light, and 'multiple emission galaxies' show multiple resolved knots of ${\rm H}\alpha$ emission connected by diffuse light. These classifications and a summary of key galaxy properties derived from optical and near infrared (NIR) data are reproduced in Table 1.

Exponential disc models were fit to the observed $H\alpha$ velocity maps of the full sample utilising a reduced chi-squared minimisation with Monte Carlo Markov Chain methods. Seven galaxies were found to be consistent with an exponential disc model when taking into account the chi-squared value of the fit and the residual of the difference between

Table 1. Summary of WiggleZ galaxy properties

WiggleZ ID	ID	Z	$SFR^a_{H\alpha}$	σ^a	$\log(\mathrm{M_{*}[M_{\odot}]})^{b}$	A_V^b	Morphological
			$(\mathrm{M}_{\odot}~\mathrm{yr}^{-1})$	$({\rm km} \; {\rm s}^{-1})$		(mag)	Type^c
R03J032450240-13550943	WK0912 _ 13R	1.2873	20.3 ± 6.8	81.6 ± 27.7	10.7 ± 0.2	1.1 ± 0.3	M^d
S15J145355248 - 00320351	WK1002 _ 61S	1.3039	35.6 ± 2.3	85.1 ± 20.3	10.7 ± 0.7	0.2 ± 0.2	M
R01J005822757-03034040	WK0909 _ 02R	1.3616	20.2 ± 3.8	87.9 ± 21.9	10.3 ± 0.6	0.7 ± 0.4	M
R03J032206214-15443471	WK0909 _ 06R	1.4602	54.8 ± 3.9	92.6 ± 27.8	11.0 ± 0.2	0.8 ± 0.3	M^d
S15J144102444+05480354	$WK0905_22S$	1.2810	44.0 ± 1.8	98.2 ± 10.9	10.3 ± 0.2	0.3 ± 0.2	E^d
R00J232217805-05473356	WK0912 _ 01R	1.2960	24.6 ± 3.2	98.6 ± 19.6	10.0 ± 0.6	0.5 ± 0.2	E^d
S09J091517481 + 00033557	WK1002_41S	1.3330	29.9 ± 2.0	91.4 ± 13.0	10.2 ± 0.1	0.4 ± 0.1	E^d
S00J233338383 - 01040629	$WK0809_02S$	1.4521	42.5 ± 7.7	92.7 ± 16.6	11.1 ± 0.6	0.0 ± 0.1	\mathbf{E}
S15J142538641 + 00483135	WK1002 _ 18S	1.3044	25.3 ± 2.1	102.1 ± 20.0	10.2 ± 0.1	0.5 ± 0.1	S^d
S11J101757445-00244002	WK1002_14S	1.3048	40.6 ± 1.9	113.7 ± 8.8	10.6 ± 0.2	0.3 ± 0.1	S^d
S09J090933680 + 01074587	WK1002 _ 46S	1.3074	22.0 ± 2.0	124.8 ± 24.9	9.8 ± 0.6	0.2 ± 0.3	S
S11J110405504+01185565	WK1002_52S	1.3191	38.6 ± 2.7	125.4 ± 20.9	11.7 ± 0.1	0.0 ± 0.1	S
S09J090312056-00273273	WK0912 _ 16S	1.3260	17.6 ± 2.0	85.1 ± 18.6	9.8 ± 0.2	0.1 ± 0.1	S

 $^{^{}a}$ H α and kinematic properties are derived from OSIRIS near-infrared observations with a BG03 IMF.

the model velocity map and observed velocity map. These fits and associated uncertainties are discussed in more detail in Section 3.6 of Wisnioski et al. (2011). The galaxies consistent with a disc model are indicated in Table 1. One galaxy, WK0905_02R, was identified as a possible merger in the Appendix of Wisnioski et al. (2011) due to a low surface-brightness optical counterpart identified at the same redshift, which extends out to 21 kpc from the brightest region of WK0905_02R detected with OSIRIS.

Dust extinctions, A_V , were estimated for all the objects in the sample from the best-fit SED using UV, optical, and NIR photometry assuming a Calzetti dust law (Calzetti et al. 2000) and are given in Table 1. This is a common technique for high-redshift galaxies however, these values can be uncertain due to poor sampling of the full SED, as will be investigated in Section 3.3.

2.2 Herschel observations

From this sample, all 13 galaxies have been observed for 1687 s with the Herschel Spectral and Photometric Imaging REceiver (SPIRE; Griffin et al. 2010) imager in the 250, 350 and 500 μ m bands. The pixel size and beam FWHM for SPIRE are 6", 10", 14" and 18.2", 24.9", 36.3" respectively for the 250, 350 and 500 μ m bands. The images are calibrated using the standard SPIRE pipeline in units of mJy/beam. The confusion limit for each band is 5.8, 6.3, and 6.8 mJy/beam. The total variance in each image is estimated by adding in quadrature the confusion noise, $\sigma_{\rm conf}$, and the instrument noise over the observation time as given by Nguyen et al. (2010).

The reduced images are calibrated such that the source flux is given by the flux in the pixel at the peak of the PSF at the expected location of the source (Nguyen et al. 2010). The fluxes of the detected WiggleZ sources were extracted by fitting a 2D Gaussian, taking the peak as the total flux as outlined in the *Source Fitting of Point Sources in Maps* recipe of the SPIRE Photometry Cookbook¹ and are given in

Table 2. The extraction includes division by the pixelisation correction factor defined in the SPIRE Observers' Manual² which corresponds to P = [0.951, 0.931, 0.902] respectively for [250, 350, 500] μ m. Additionally, the appropriate correction has been made to the 350 μ m fluxes in the cases in which the data was reduced with the out of date version of the reduction pipeline HIPE V5¹. Errors on source flux values are given by adding in quadrature the total image variance with the error on the peak flux value determined from the 2D Gaussian fitting with the error extension used as the corresponding error image in the fit.

Detections at 3σ confidence are defined by the flux limit $3 \times \sigma_{\rm conf}$, or > 17.4 mJy, > 18.9 mJy, and > 20.4 mJy for the 250, 350 and 500 μ m bands. Only three of the thirteen objects observed, WK0909_02R, WK0909_06R, and WK0912_13R, are detected in more than two wavebands. For non-detected sources upper-limits are quoted as $3\sigma_{\rm conf}$. Tri-colour images created from the three SPIRE bands are shown in Fig. 1 for the detections. Fluxes for the detected galaxies are given in Table 2.

2.3 Deblending with WISE

Due to the large pixels and beam sizes, many astronomical sources may overlap within one SPIRE beam. The near neighbours can contaminate source extraction giving inaccurate flux measurements. Higher resolution 4.6 μ m images, with spatial resolution of 6.4"/pixel, from the Widefield Infrared Survey Explorer (WISE; Wright et al. 2010) all-sky survey (Cutri & et al. 2012) are used as a prior to determine precise locations of sources nearby to the target WiggleZ galaxies (e.g. Labbé et al. 2006; Wuyts et al. 2007; Whitaker et al. 2011), and to check the Herschel and OSIRIS astrometry. Within the all-sky WISE data release the three Herschel detected galaxies from this sample are

July 2011) available at: http://herschel.esac.esa.int/hcss-doc-10.0 /load/spire_drg/html/spire-photometer.html

^b Values derived from SED fitting to UV, optical, and NIR magnitudes with a BG03 IMF.

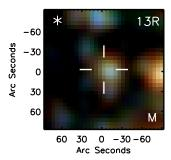
^c Morphological classification based on 0.05'' H α imaging with OSIRIS; M: multiple emission, E: extended emission, S: single emission.

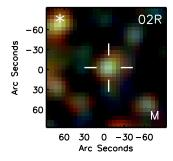
 $[^]d$ H α velocity map consistent with a model exponential disc.

 $^{^{1}\,}$ The SPIRE Photometry Cookbook (Bendo et al. 2011; version

² The SPIRE Observers' Manual available at:

4 Wisnioski et al.





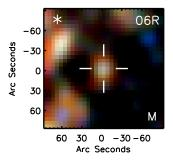


Figure 1. RGB images made from the three SPIRE bands ($250\mu m:blue, 350\mu m:green, 500\mu m:red$). Each image is 3 arc min on a side. The images are centred on the expected position of the WiggleZ galaxies based on optical astrometry and confirmed by high resolution near-infrared images. The H α morphology is given in Table 1 and denoted in the bottom right corner of each image.

Table 2. Herschel SPIRE observations and dust properties of WiggleZ galaxies

ID	f ₂₅₀ (mJy)	f ₃₅₀ (mJy)	f ₅₀₀ (mJy)	$\log(\mathrm{L_{IR}[L_{\odot}]})$	T _{dust} (K)	$\log(\mathrm{M_{dust}[M_{\odot}]})$	$A_{H\alpha}^b$ (mag)	$\frac{\mathrm{SFR}_{\mathrm{corr}}^{\mathrm{H}\alpha,b}}{(\mathrm{M}_{\odot}\ \mathrm{yr}^{-1})}$
WK0912_13 R^a	18.72 ± 5.93	25.53 ± 6.43	17.63 ± 6.99	11.8 ± 0.1	21.6 ± 4.4	9.4 ± 0.4	0.92	48
WK0909_02R	25.85 ± 5.90	21.46 ± 6.40	12.02 ± 6.95	12.1 ± 0.3	29.8 ± 8.4	9.0 ± 1.3	1.40	73
WK0909_06R	36.09 ± 5.90	33.47 ± 6.39	23.22 ± 6.92	12.3 ± 0.1	27.5 ± 4.0	9.3 ± 0.2	0.96	132

^a Objects with FIR properties derived from deblended sources as outlined in Section 2.3.

detected in at least one of the four WISE wavebands. Of the galaxies detected with Herschel only one, WK0912_13R, is confused by nearby sources in the Herschel images. Figure 2 shows the tri-colour image of WK0912_13R using near infrared IRIS2 Ks-band images (blue contours), WISE 4.6 μm images (green), and SPIRE 250 μm images (red). The 4.6 μm and 250 μm images are selected for this image because they have the highest resolution and highest detection fraction for the WiggleZ kinematic sample.

An attempt is made to deblend the nearby sources from the expected location of WK0912_13R using the WISE $4.6\mu m$ image. In the left panel of Fig 2, two WISE sources are co-located with the SPIRE 250 μm beam near the expected location of the WiggleZ galaxy. Assuming these two sources contribute to the 250 μ m emission, one being the WiggleZ source and the other a bright nearby source $\sim 15''$ south-west of the expected location of the WiggleZ galaxy. These locations are then fixed within the image and a SPIRE source is modelled at each location by a two-dimensional Gaussian with FWHM of the SPIRE beam to represent the PSF of these images. A Gaussian provides a good estimate of the shape of the SPIRE beam. A chi-squared minimisation of the difference of the data and the model is conducted using downhill simplex methods with the flux of each modelled source as the only free parameters. The model image of the neighbouring source is then subtracted from the actual image and a flux is extracted from the residual at the expected WiggleZ position by the same method described in Section 2.2. The deblended image of WK0912_13R is shown in the right panel of Fig. 2. The tricolour SPRIE image reveals a similar colour as WK0909_02R and WK0909_06R, suggesting that the deblending has been successful. The resulting fluxes are $3.2\sigma_{\rm conf}$, $4.1\sigma_{\rm conf}$, and $2.6\sigma_{\rm conf}$ in the 250,

350, and 500 $\mu \rm m$ bands respectively, and are given in Table 2.

2.4 Stacking

The ten non-detected sources were stacked to put a limit on the typical infrared luminosity and dust content on the remainder of the WiggleZ kinematic sample. The stacking technique follows from Rodighiero et al. (2010) and Magdis et al. (2010) and is described shortly here. First, $60'' \times 60''$ images were extracted around each object in the three SPIRE bands. Because of the large pixel sizes of the SPIRE images, sub-pixel shifts were applied in an effort to best recover the stacked emission without smearing a detection. The shifts were performed using a Fourier transform interpolation. To avoid image defects and correlations arising from the coverage pattern each image was rotated 90° relative to the previous image in the stack. The images were then median-combined to construct a final stacked image in each band. Signal is detected in the 250 μ m band stack at 6.1 mJy. Perhaps surprisingly, no flux is detected above the confusion noise in the stacks of the 350 or 500 μ m bands. This is attributed to the low number statistics of the sample. Upper limits are derived in each band at $z \sim 1.32$ from the stacked images resulting in < 5.2 mJy and < 5.1 mJy for the 350, and 500 μ m bands respectively.

3 RESULTS & ANALYSIS

3.1 Detections vs. non-detections

The three detected galaxies have the largest H α sizes ($r_{1/2} \ge 4$ kpc), the highest expected dust extinctions ($A_{\rm V} \ge 0.7$

^b Derived from the ratio of infrared and $H\alpha$ luminosities using the prescription of Kennicutt et al. (2009).

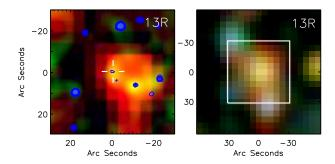


Figure 2. (left) RGB image made from SPIRE 250μm (red), WISE W2-4.6μm (green), and near-infrared IRIS2 Ks (blue contours) images of WK0912-13R. A bright nearby source confuses the possible detection of the WiggleZ target as seen by the bright 4.6 μm source $\sim 15''$ south-west of the expected location of the WiggleZ galaxy. (right) Deblended RGB image of WK0912-13R created from SPIRE bands (250μm, 350μm, 500μm). The neighbouring source was modelled and removed in each SPIRE band to create this deblended image of the galaxy. The remaining flux is detected at the WiggleZ position above $3\sigma_{\rm conf}$ in the 250 and 350 μm bands. The white box indicates the zoomed-in region shown in the left image

mag) and are massive $(\log(M_*[\mathrm{M}_\odot]) \geqslant 10.7)$. They do not correlated to the highest $\mathrm{H}\alpha$ SFR or specific SFR objects. The three detections show the largest velocity shear within the sample corresponding to two disc galaxies and one merger. None of the compact $(r_{1/2} \sim 1-2~\mathrm{kpc})$ or 'dispersion dominated' galaxies were detected. The other nondetected disc galaxies all have sizes of $\leqslant 3~\mathrm{kpc}$ and estimated global dust extinctions of $\leqslant 0.5~\mathrm{mag}$. The implications of the kinematics of the detections vs. non detections is discussed in more detail in Section 4. As expected, and in agreement with the PACS detected LBGs at z=0.8-1.2 (Oteo et al. 2013) the WiggleZ SPIRE detections are also the reddest objects in the sample as probed by their UV-NIR SEDs shown in Fig. 3.

3.2 Dust properties

To obtain infrared luminosities and dust temperatures a blackbody emission curve in the optically thin approximation, or graybody, was fit to the measured SPIRE fluxes given in Table 2 defined by,

$$S_{\nu} \propto \frac{\nu^{3+\beta}}{exp(h\nu/kT_{\rm d}) - 1},$$
 (1)

where S_{ν} is the observed flux density at frequency ν , h is the Planck constant, k is the Boltzmann constant, $T_{\rm d}$ is the dust temperature, and the dust emissivity spectral index is set to $\beta=1.5$. A degeneracy exists between the dust emissivity and dust temperature in the case where only limited frequency measurements are available, as such β is held constant (Blain et al. 2003). The value of β is not well constrained, ranging from 1.5 – 2.0 for high-redshift galaxies. Our results are relatively insensitive to the choice of β with the difference in $T_{\rm d}[K]$ of $\Delta T_{\rm d}=4$ and a difference in $L_{\rm IR}$ of $\Delta \log(L_{\rm IR}[L_{\odot}])=0.04$ when $\beta=2.0$, comparable to the statistical errors. This simple model has been shown to give

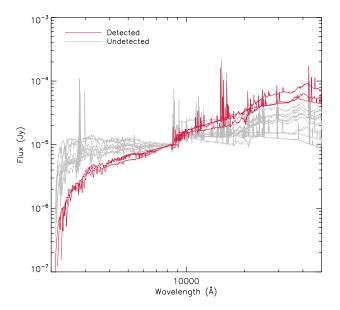


Figure 3. Ultraviolet to near infrared SED fits for detected (red) and non-detected sources (gray) reveal that the three detected sources have the reddest UV SEDs of the WiggleZ kinematic sample. Small variations in the flux level of the SEDs are normalised to a common flux value at $8 \times 10^3 \mathring{A}$.

reliable measurements of dust properties for sparsely sampled SEDs (e.g. Blain et al. 2002, 2003; Kovács et al. 2006; Pope et al. 2006).

For the WiggleZ detections at $z\sim1.3$, the three SPIRE bands constrain the turnover of the graybody providing a reliable estimate of the dust temperature. The best-fit graybody is shown in Fig. 4 for the three detected WiggleZ sources, with values obtained for $T_{\rm d}=[21.6,\ 29.8,\ 27.5]$ K, and $\log(L_{\rm IR}[{\rm L}_{\odot}])=[11.8,\ 12.1,\ 12.3]$ for WK0912_13R, WK0909_02R, and WK0909_06R respectively. Far-infrared SEDs were fit to the WISE and Herschel photometry to show the overall shape of IR SED using the Dale & Helou (2002) templates, which are shown in Fig. 4 with the UV-NIR photometry and SED fits.

A Monte-Carlo analysis is performed to measure errors on $T_{\rm d}$ and $L_{\rm IR}$ by varying the SPIRE fluxes within a Normal distribution around the measured value. The derived values for WK0912_13R and WK0909_06R are well determined as the three SPIRE points probe the full turn over. The derived values for WK0909_02R are much more uncertain, $\sigma(T_{\rm d}) \sim 9$ K, as the measured 250 μ m flux less clearly probes the Wein side of the blackbody curve. We note here that the results from staking analysis indicate that the non-detections have warmer dust as the 250 μ m, 350 μ m and 500 μ m imply a descending slope as expected on the Wein side of the blackbody curve.

The stacking analysis of Section 2.4 yields a detection for the 250 μm band and upper limits for the two long wavelength bands suggesting that on average the SPIRE bands probe the Rayleigh-Jeans side of the graybody curve for the non-detections. This assumption allows for a determination of lower limits on the dust temperature and infrared luminosity of $T_{\rm d} > 27~{\rm K}$ and $\log(L_{\rm IR}[L_{\odot}]) > 11.3$ respectively. Figure 4 shows the average SED for the non-detections in-

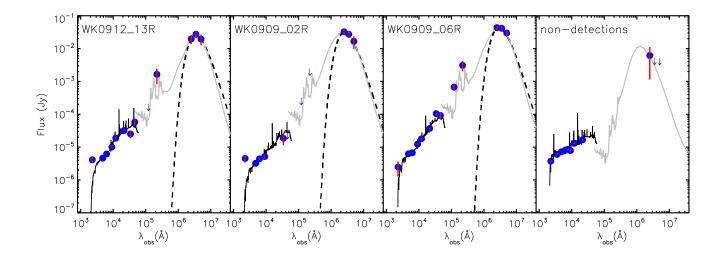


Figure 4. Infrared spectral energy distributions of the three detected WiggleZ sources, WK0912_13R, WK0909_02R, and WK0909_06R, and the average spectral energy distribution of the non-detections. The blue points are the observed UV to FIR fluxes of the galaxies and downward pointing arrows indicated limits. The dashed black line is the best-fit graybody curve to the SPIRE photometry used to derive dust properties, as described in Section (3.2). SED fits to the UV to NIR from Wisnioski et al. (2011) and SED fits to the MIR to FIR using templates from Dale & Helou (2002) are shown by the solid black and gray curves, respectively.

cluding the stacking results. One possible FIR SED model is shown from Dale & Helou (2002) for comparison to the SEDs of the detected galaxies.

Comparison samples in the WiggleZ detections redshift range (1.2 < z < 1.6) with FIR measurements include star-forming galaxies (LBGs: Burgarella et al. 2011; 'main-sequence' galaxies: Magnelli et al. 2012b), starbursts (Casey et al. 2012), and SMGs (Swinbank et al. 2004; Chapman et al. 2010; Magnelli et al. 2012a), where the value of dust emissivity is constant across these samples $(\beta=1.5)$. The starbursts and SMGs have average $T_{\rm d}\sim 30-50$ K and $L_{\rm IR}\gtrsim 10^{12.5}$ L $_{\odot}$. More typical star-forming galaxies are considerably more difficult to detect, as reiterated by this work. As a result there are only four individual galaxies at this redshift for comparison, with $T_{\rm d} \sim 34$ K and $L_{\rm IR} \sim 6 \times 10^{11}$ L $_{\odot}$ (Burgarella et al. 2011; Magnelli et al. 2012b). A comparison with these samples suggests that derived infrared properties for the WiggleZ sample (from the detections and implied from the nondetections), are reflective of 'average' or main-sequence systems, in agreement with the conclusions drawn from their $H\alpha$ properties (Wisnioski et al. 2011). The differences of $L_{\rm IR}$ and $T_{\rm d}$ between galaxy populations at $z\sim 1.4$ are consistent with studies at lower redshifts and in highredshift survey fields, where a more statistical study of the $T_{\rm d}-L_{\rm IR}$ plane is possible (e.g. Chapman et al. 2003; Hwang et al. 2010; Roseboom et al. 2011; Magnelli et al. 2012a; Symeonidis et al. 2013). However, these distinctions (particularly at z > 1), can be biased by the detection limits of current and past infrared facilities (e.g. Magnelli et al. 2012a; Casey et al. 2012).

Dust masses are estimated from the modified blackbody such that,

$$M_{\text{dust}} = \frac{S_{\nu} D_L^2}{(1+z)\kappa_{\text{rest}} B_{\nu}(\lambda_{\text{rest}}, T_{\text{dust}})},\tag{2}$$

where the dust mass absorption coefficient κ_{rest} is given by

$$\kappa_{\text{rest}} = \kappa_{\text{obs}} (\frac{\lambda_{\text{obs}}}{\lambda_{\text{rest}}})^{\beta},$$
(3)

 B_{ν} is the Planck function at frequency ν , and D_L represents the luminosity distance. Following Li & Draine (2001), $\kappa_{\rm obs}$ is set to 0.517 m² kg⁻¹ for observed wavelength 250 μ m. The estimated dust masses are $\log(M_{\rm dust}[{\rm M}_{\odot}]) = [9.3, 9.4, 9.0]$ for WK0912_13R, WK0909_02R, and WK0909_06R respectively. Statistical errors are measured using the Monte Carlo techniques described above and are given in Table 2. These values are also uncertain due to the assumptions of both β and $\kappa_{\rm obs}$. The choice of $\beta=2$, rather than $\beta=1.5$ used here, results in higher dust masses such that $\Delta \log(M_{\rm dust})=0.1$, within the statistical errors. Furthermore, the blackbody fitting method used to estimate the dust mass has been shown to give masses a factor of 2 lower than an alternative method using the models from Draine & Li (2007) (Magdis et al. 2012).

Recent works have derived gas masses by assuming that gas mass is proportional to dust mass at a given metallicity (e.g. Leroy et al. 2011; Magdis et al. 2012; Magnelli et al. 2012b). While these methods are uncertain (e.g. due to the reliability of metallicity estimates and assuming simple dust model used here) they are applied to the WiggleZ detections to derive approximate gas masses and thus gas fractions. Using the relation from Leroy et al. (2011),

$$\log \delta_{\rm GDR} = (9.4 \pm 1.1) - (0.85 \pm 0.13)[12 + \log({\rm O/H})], \quad (4)$$

and the metallicities derived from the [NII]/H α from Wisnioski et al. (2011), gas-to-dust ratios, $\delta_{\rm GDR} \equiv M_{\rm gas}/M_{\rm dust}$, are estimated in the range 135-160. Gas fractions, $f_{\rm gas}$, are estimated as $\sim \! 0.86$, 0.94, and 0.57 for

WK0912_13R, WK0909_02R, and WK0909_06R respectively where $f_{\rm gas} = M_{\rm gas}/(M_{\rm gas} + M_*)$. At $z \sim 1.5$ the estimated values for WiggleZ galaxies are in broad agreement with gas fractions for main sequence galaxies at the same redshift as estimated from CO emission (Daddi et al. 2010; Tacconi et al. 2010).

3.3 Correcting for dust extinction

Observed luminosities and star formation rates derived from the ${\rm H}\alpha$ and infrared observations are compared in order to estimate the attenuation from intervening dust and to bring the near-infrared and far-infrared global SFR indicators into agreement. Infrared luminosities are commonly used to derive more accurate estimates of the true SFR of a galaxy by assuming that all ${\rm H}\alpha$ light attenuated by dust is re-emitted in the infrared (Devereux & Young 1990; Inoue et al. 2001). This assumption is dependent on the nature (and uniformity) of the dust and the stellar population responsible for heating the dust. Nonetheless, assuming that infrared radiation for SFGs results from young stars and the stellar radiation field (Calzetti et al. 2000), the infrared luminosities for the WiggleZ galaxies are used to estimate reddening and dust attenuation.

Total SFRs as derived from the infrared have traditionally been estimated using the theoretical prescription of Kennicutt (1998b) for $L_{\rm IR}[8\text{-}1000~\mu{\rm m}]$. However, this prescription was designed for starbursts (continuous bursts of age 10 - 100 Myr) and although it has been shown to be accurate for a range of galaxy populations (Kewley et al. 2002), it can systematically over-estimate total SFRs (Kennicutt et al. 2009; Nordon et al. 2010). Results from recent infrared facilities have led to tighter conversions from $L_{\rm IR}$ to SFR. Unfortunately, most new SFR prescriptions require information from single wavebands particular to each infrared facility (e.g. 8 μ m or 24 μ m) which are not available for the WiggleZ sample (e.g. Calzetti et al. 2005; Relaño et al. 2007; Rieke et al. 2009). However, these have been brought together for a generalised total IR/H α SFR indicator by combining IRAS and Spitzer data for star-forming galaxies at z = 0 from the SINGS survey (Kennicutt et al. 2009).

This prescription is used to estimate the dust attenuation and total SFRs using $L_{\rm IR}$ and $L_{\rm H\alpha}$ for the WiggleZ kinematic sample. It is noted that (1) both prescriptions are calibrated on local star-forming galaxies and thus may not be applicable to this $z\sim 1.3$ sample and (2) as no continuum is detected in the OSIRIS observations an assumption is made that there is no underlying ${\rm H}\alpha$ stellar absorption. This method uses an empirical prescription to estimate dust extinction in the form of,

$$A_{\rm H\alpha} = 2.5 \log \left[1 + \frac{a_{\lambda} L_{\lambda}}{L_{\rm H\alpha}} \right], \tag{5}$$

which can be used to calculate a dust corrected luminosity from a linear combination of $H\alpha$ luminosity and luminosities from a variety of infrared indicators,

$$L_{\mathrm{H}\alpha}^{\mathrm{corr}} = L_{\mathrm{H}\alpha}^{\mathrm{obs}} + a_{\lambda} L_{\lambda},\tag{6}$$

$$SFR_{H\alpha}^{corr}[M_{\odot} \text{ yr}^{-1}] = 7.9 \times 10^{-42} L_{H\alpha}^{corr}[\text{ergs s}^{-1}]$$
 (7)

where λ in this case is represented by the total infrared lumi-

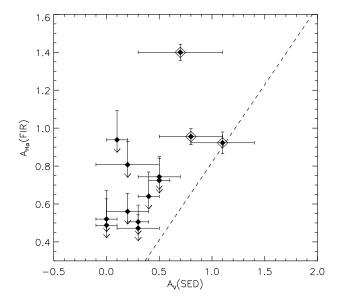


Figure 5. Comparison of extinctions A_V , derived from UV-optical-NIR SED fitting, and $A_{\rm H\alpha}$ derived from $L_{\rm IR}/L_{\rm H\alpha}$ using the empirical results of Kennicutt et al. (2009). The dashed line represents the relationship between A_V and $A_{\rm H\alpha}$ using the galactic obscuration curve of Calzetti et al. (2000). The detections are represented by outlined diamonds. The upper limits for the non-detections are derived from fitting modified blackbody curves to $3 \times \sigma_{\rm conf}$ holding both $T_{\rm d}$ constant (top of $A_{\rm H\alpha}$ error bar) and $L_{\rm IR}$ constant (diamond) to the average values of these parameters derived from the detections.

nosity, TIR[3-1100 μ m], with the corresponding scaling coefficient, found empirically to be $a_{\rm TIR}=0.0024\pm0.0006$ and the attenuation in H α represented by $A_{\rm H}\alpha$. The definition of TIR[3-1100 μ m] (Kennicutt et al. 2009) differs slightly from the adopted range in this paper, IR[8-1000 μ m], this slight difference is assumed to have a negligible effect on $a_{\rm TIR}$.

As expected the SFR derived directly from the $H\alpha$ gives a lower estimate of the total SFR than the far-infrared, with $SFR_{IR}/SFR_{H\alpha} \sim 4$, using the Kennicutt (1998a,b) SFR conversions. The Kennicutt et al. (2009) prescription brings the two star formation rate indicators ($L_{\mathrm{H}\alpha}^{\mathrm{corr}}$ and L_{IR}) in better agreement within a factor of $SFR_{IR}/SFR_{H\alpha}^{corr} \sim 1.5$. The new SFR values, ${\rm SFR}^{\rm corr}_{{\rm H}\alpha},$ are given in Table 2. One possible contributor to the discrepancy between the two indicators is the relatively low metallicity of the WiggleZ galaxies, $12 + \log(O/H) \sim 8.5$, which could bias the ratio of SFRs (Roseboom et al. 2012; Domínguez et al. 2012). However it is noted, the galaxy with the most discrepant $L_{\rm IR}$ and $L_{\rm H\alpha}$ is WK0909_02R. Optical imaging of WK0909_02R indicates that the OSIRIS H α luminosity is underestimated due to an aperture effect as multiple components of the system cover ~ 4 arc seconds, comparatively larger than the field of view of OSIRIS. In contrast, the SPIRE beam would encompass the whole system, accounting for the difference in SFR indicators. This aperture effect should be negligible for WK0909_06R, and WK0912_13R as they appear to be disc galaxies with the bulk of $H\alpha$ detected within the OSIRIS field of view.

The FIR derived $A_{\rm H\alpha}$ values of the three WiggleZ

galaxy detections ($A_V \sim 1-2$ mag) are comparable to other z>1 galaxy extinction measurements (e.g. Glazebrook et al. 1999; Ibar et al. 2013) and in line with $A_V \sim 1$ mag normally assumed for local SFGs (Kennicutt 1992; Tresse et al. 1996; Calzetti 2001), whereas dust in more extreme systems, i.e. SMGs, can suppress the observed star formation rate by a factor of 10 (Swinbank et al. 2004).

In comparison, the dust correction derived from the UV-NIR SEDs leave the corrected H α SFRs over a factor of SFR $_{\rm H}^{\rm corr,IR}/{\rm SFR}_{\rm H}^{\rm corr,SED}\sim 1.5$ discrepant. This comparison can be seen in Fig. 5 between far-infrared derived $A_{\rm H}\alpha$ and UV-NIR SED derived A_V . For the WiggleZ galaxies, the attenuation derived by SED fitting are systematically underestimated, as the three detected objects have the highest values of dust attenuation from the UV-NIR fits, $A_V>0.6$ mags.

4 KINEMATIC IMPLICATIONS OF HERSCHEL OBSERVATIONS

From $H\alpha$ morphologies, the three detected objects are classified as 'multiple emission' galaxies with two, WK0909_06R and WK0912_13R, being the largest disc galaxies in the sample containing resolved star-forming regions, reminiscent of local HII regions (Wisnioski et al. 2012). No 'compact emission' galaxies were detected. The results of this analysis could be used to support the conclusion that the multiple emission galaxies are mergers based upon, 1.) mergers are a common mechanism to drive-up $L_{\rm IR}$ – e.g. ULIRGs and SMGs 2.) the clumpy structure could be a result of dust variation across the galaxy rather than the true structure of the young stars, and 3.) there is some overlap of the $L_{\rm IR}$ - $T_{\rm d}$ values between the WiggleZ results and SMGs. However, WK0909 $_06R$ and WK0912 $_13R$ have infrared luminosities of $\sim 1 \times 10^{12} L_{\odot}$, an order of magnitude lower than most typical $z \sim 2$ SMGs that are known to be mergers. Some observations also suggest that some 'cold' SMGs (< 20 K) are contaminated by nearby sources, biasing luminosity derivations and underestimating temperatures (Hwang et al. 2010). Yet, at this $L_{\rm IR}$ the fractional contribution of spirals is expected to be less (25%) than of major mergers (40%). These percentages however are based on a wide redshift range z = 0.1 - 3.5 and thus likely integrates over an evolution in luminosity and galaxy type (Kartaltepe et al. 2010b). Combining the kinematic results and $H\alpha$ clump analysis for the disc galaxies it is more likely that these results indicate that the far-infrared emission originates from the same young stellar populations that generates the H α emission, namely the star-forming clumps identified in Wisnioski et al. (2012) which enhance the stellar radiation field in the multiple emission galaxies, increasing the likelihood of detection with Herschel (e.g. Zurita et al. 2000; Kewley et al. 2002). The other disc-like galaxies, which do not show large clumps, are undetected.

However, following this assumption a detection is expected for WK1002_61S, the only other galaxy classified as having multiple regions of emission in this sample, which has an H α luminosity $\sim 2\times$ the H α luminosity of WK0909_02R and WK0912_13R. The galaxy WK1002_61S has $2\sigma_{\rm conf}$ detections in the 350 $\mu{\rm m}$ and 500 $\mu{\rm m}$ SPIRE bands. It is possible that inclination may have an effect. However, from H α

morphologies this object looks most edge-on of the four multiple emission galaxies, implying a greater dust extinction (e.g. Holmberg 1975; Shao et al. 2007). Deep optical broadband imaging is needed to get a more complete morphological picture of this object.

None of the compact $(r_{\rm eff} \sim 1 \text{ kpc})$ 'single emission' galaxies are detected with Herschel. A possible interpretation is that these galaxies are consistent with undergoing a starburst or AGN mode. If these objects were starbursts resultant from mergers they would be expected to lie above the 'main sequence' of star-formation, be more compact than main sequence galaxies, and have warmer dust temperatures ($T_{\rm d} \sim 40$ K; Elbaz et al. 2011). These properties are broadly consistent with what is observed here, however the infrared luminosity of the non-detections is not constrained and thus their offset from the main-sequence is unknown. Although these galaxies do not show properties of hosting an AGN in their optical-NIR spectra (Wisnioski et al. 2011), they may contain dust enshrouded AGN. However, the observed wavebands of this study do not probe the mid infrared where the broadband SED of AGN systems peak (Hatziminaoglou et al. 2010; Kirkpatrick et al. 2012).

Alternatively, If the infrared luminosities of the non-detected compact single emission galaxies are low, $\sim 5\times 10^{11}$ L_{\odot} , with dust temperatures of ~ 30 K (just below our detection limit) then they may be consistent with pseudo-bulges of young discs possibly forming after the coalescence of clumps in clumpy discs (Elmegreen et al. 2008). Indeed, the single-clump objects show the highest velocity dispersions (Table 1) which is qualitatively in agreement with the bulge formation models of (Bournaud & Elmegreen 2009). Another possible scenario is that they are compact discs that are unresolved even with adaptive-optics aided ~ 750 pc resolution (Newman et al. 2012).

The kinematic/FIR results presented here are in agreement with what has been derived from morphologies of star-forming galaxies with FIR detections (Magnelli et al. 2012b; Oteo et al. 2013). The only other sample with published H α IFS kinematics and FIR properties at z>1 is a sub-millimeter sample of three galaxies. These galaxies at z=[1.4,2.2,2.3], originally detected at 850 μ m with SCUBA, have hot dust temperatures of $\sim 35-55$ K and infrared luminoities of $9-60\times10^{12}$ L $_{\odot}$ (Menéndez-Delmestre et al. 2013; Chapman et al. 2005). The H α properties and kinematics support the hypothesis that the objects are mergers or starbursts showing broad H α line widths, high star formation surface densities and no evidence for rotation.

5 CONCLUSIONS

In the UV-selected WiggleZ kinematic sample, three of thirteen galaxies are detected at the 3σ level with Herschel/SPIRE. The dust SEDs of the three detected galaxies are dominated by cold dust ($T_{\rm d} \sim 26~{\rm K}$) consistent with the ISM heating by the UV and interstellar radiation field. Modified blackbody fits reveal average infrared luminosities and dust masses of $L_{\rm IR} \sim 1.2 \times 10^{12}~{\rm L}_{\odot}$ and $M_{\rm dust} \sim 9.2~{\rm M}_{\odot}$ respectively, yielding inferred gas fractions of > 50%. The FIR results of the sample are in agreement with the interpretation of the NIR H α kinematic data, showing the strength of combing multi-wavelength data with integral field spec-

troscopy for a more complete understanding of the kinematics and formation of individual galaxies.

In this sample, two of the detected sources are likely disc galaxies and one a starburst resulting from a merger. The two disc candidates have the largest spatial extent within the sample and contain multiple regions of emission, suggesting that the cold dust detected is a result of heating of the interstellar radiation field by the clumps. The other detection is more likely to be a starburst resulting from an ongoing merger. This assumption is supported by broadband imaging and long-slit spectroscopy that confirms that there are two close companions to the brightest knot of H α emission. The compact single emission galaxies, not detected in the FIR. Stacking analysis reveals that they likely have warmer dust temperatures, $T_{\rm d} > 27$, on average than the detected objects. The combination of the kinematic and FIR data suggest that they may be pseudo-bulges in a later phase of clumpy disc formation, however a starburst or AGN mode can not be ruled out.

The data presented here are among the few individual main-sequence star-forming galaxies to be detected at high redshift in the far infrared with Herschel-SPIRE (Elbaz et al. 2011; Burgarella et al. 2011; Magnelli et al. 2012b). They confirm the stacked results of Reddy et al. (2012) that typical UV-selected galaxies have analogous dust properties as local LIRGs and LBGs at z 1 (Burgarella et al. 2011) and have comparable infrared properties to $z \sim 1$ samples of star-forming galaxies (Domínguez et al. 2012; Magnelli et al. 2012b). The average attenuation of the detected galaxies is $A_{\rm H\alpha} = 1.1 \text{ mag}$ or $A_V = 0.9$ mag, assuming a Calzetti et al. (2000) obscuration curve, leading to dust corrected H α star-formation rates of \sim 3× the observed ${\rm H}\alpha$ star formation rates. The non-detections have an attenuations $A_{\rm H\alpha} < 0.76$ mag, when fixing the dust temperature.

Resolved dust properties are a key measurement needed to understand the thick clumpy discs at high redshift and the complexity and impact of mergers. With the end of the Herschel mission the next step forward will be the comparison of FIR properties from ALMA with z>1 resolved galaxy kinematics. Future kinematic surveys may also find overlap with detections from the deeper Herschel surveys, especially at $z\lesssim 1$. The upcoming KMOS^{3D} survey in the deep fields is one such example.

ACKNOWLEDGMENTS

We would like the thank the referee for valuable comments. EW is very grateful to B. Magnelli, D. Lutz, and J. T. Mendel for useful conversations. AMS gratefully acknowledges an STFC Advanced Fellowship through grant $\rm ST/H005234/1$.

This paper used data from the Herschel Space Telescope. The Herschel spacecraft was designed, built, tested, and launched under a contract to ESA managed by the Herschel/Planck Project team by an industrial consortium under the overall responsibility of the prime contractor Thales Alenia Space (Cannes), and including Astrium (Friedrichshafen) responsible for the payload module and for system testing at spacecraft level, Thales Alenia Space (Turin) responsible for the service module, and Astrium

(Toulouse) responsible for the telescope, with in excess of a hundred subcontractors.

REFERENCES

Baldry, I. K., & Glazebrook, K. 2003, ApJ, 593, 258
Blain, A. W., Barnard, V. E., & Chapman, S. C. 2003, MNRAS, 338, 733

Blain, A. W., Smail, I., Ivison, R. J., Kneib, J.-P., & Frayer, D. T. 2002, Phys. Rep., 369, 111

Bournaud, F., & Elmegreen, B. G. 2009, ApJL, 694, L158 Burgarella, D., et al. 2011, ApJL, 734, L12

Calzetti, D. 2001, PASP, 113, 1449

Calzetti, D., Armus, L., Bohlin, R. C., Kinney, A. L., Koornneef, J., & Storchi-Bergmann, T. 2000, ApJ, 533, 682

Calzetti, D., et al. 2005, ApJ, 633, 871

Casey, C., et al. 2012

Chapman, S. C., Blain, A. W., Smail, I., & Ivison, R. J. 2005, ApJ, 622, 772

Chapman, S. C., Helou, G., Lewis, G. F., & Dale, D. A. 2003, ApJ, 588, 186

Chapman, S. C., et al. 2010, MNRAS, 409, L13

Cutri, R. M., & et al. 2012, Vizie
R Online Data Catalog, 2311, 0

Daddi, E., et al. 2010, ApJ, 713, 686

—. 2007, ApJ, 670, 156

Dale, D. A., & Helou, G. 2002, ApJ, 576, 159

Devereux, N. A., & Young, J. S. 1990, ApJL, 350, L25

Domínguez, H., et al. 2012

Draine, B. T., & Li, A. 2007, ApJ, 657, 810

Drinkwater, M. J., et al. 2010, MNRAS, 401, 1429

Elbaz, D., et al. 2011, A&A, 533, A119

Elmegreen, B. G., Bournaud, F., & Elmegreen, D. M. 2008, ApJ, 688, 67

Engel, H., et al. 2010, ApJ, 724, 233

Glazebrook, K., Blake, C., Economou, F., Lilly, S., & Colless, M. 1999, MNRAS, 306, 843

Gordon, K. D., Calzetti, D., & Witt, A. N. 1997, ApJ, 487, 625

Griffin, M. J., et al. 2010, A&A, 518, L3+

Hatziminaoglou, E., et al. 2010, A&A, 518, L33

Holmberg, E. 1975, Magnitudes, Colors, Surface Brightness, Intensity Distributions Absolute Luminosities, and Diameters of Galaxies, ed. Sandage, A., Sandage, M., & Kristian, J. (the University of Chicago Press), 123

Hwang, H. S., et al. 2010, MNRAS, 409, 75

Ibar, E., et al. 2013, ArXiv e-prints

Inoue, A. K., Hirashita, H., & Kamaya, H. 2001, ApJ, 555, 613

Ishida, C. M. 2004, PhD thesis, UNIVERSITY OF HAWAI'I

Kartaltepe, J. S., et al. 2011, ArXiv e-prints

—. 2010a, ApJ, 709, 572

—. 2010b, ApJ, 721, 98

Kennicutt, Jr., R. C. 1992, ApJ, 388, 310

—. 1998a, ARA&A, 36, 189

—. 1998b, ApJ, 498, 541

Kennicutt, Jr., R. C., et al. 2009, ApJ, 703, 1672

Kewley, L. J., Geller, M. J., Jansen, R. A., & Dopita, M. A. 2002, AJ, 124, 3135

Kirkpatrick, A., et al. 2012, ApJ, 759, 139

Kovács, A., Chapman, S. C., Dowell, C. D., Blain, A. W., Ivison, R. J., Smail, I., & Phillips, T. G. 2006, ApJ, 650, 592

Labbé, I., Bouwens, R., Illingworth, G. D., & Franx, M. 2006, ApJL, 649, L67

Leroy, A. K., et al. 2011, ApJ, 737, 12

Li, A., & Draine, B. T. 2001, ApJ, 554, 778

Magdis, G. E., et al. 2012

Magdis, G. E., et al. 2010, ApJL, 720, L185

Magnelli, B., et al. 2012a, ArXiv e-prints

—. 2012b, A&A, 548, A22

Menéndez-Delmestre, K., Blain, A. W., Swinbank, M., Smail, I., Ivison, R. J., Chapman, S. C., & Gonçalves, T. S. 2013, ArXiv e-prints

Newman, S. F., et al. 2012, ArXiv e-prints

Nguyen, H. T., et al. 2010, A&A, 518, L5+

Nordon, R., et al. 2010, A&A, 518, L24

Oteo, I., et al. 2013, ArXiv e-prints

Pilbratt, G. L., et al. 2010, A&A, 518, L1+

Pope, A., et al. 2006, MNRAS, 370, 1185

Reddy, N., et al. 2012, ApJ, 744, 154

Relaño, M., Lisenfeld, U., Pérez-González, P. G., Vílchez, J. M., & Battaner, E. 2007, ApJL, 667, L141

Rieke, G. H., Alonso-Herrero, A., Weiner, B. J., Pérez-González, P. G., Blaylock, M., Donley, J. L., & Marcillac, D. 2009, ApJ, 692, 556

Rodighiero, G., et al. 2010, A&A, 518, L25+

Roseboom, I., et al. 2011

Roseboom, I. G., et al. 2012, MNRAS, 426, 1782

Sanders, D. B., & Mirabel, I. F. 1996, ARA&A, 34, 749

Sanders, D. B., Soifer, B. T., Elias, J. H., Madore, B. F., Matthews, K., Neugebauer, G., & Scoville, N. Z. 1988, ApJ, 325, 74

Shao, Z., Xiao, Q., Shen, S., Mo, H. J., Xia, X., & Deng, Z. 2007, ApJ, 659, 1159

Soifer, B. T., Helou, G., & Werner, M. 2008, ARA&A, 46, 201

Swinbank, A. M., et al. 2008, MNRAS, 391, 420

Swinbank, A. M., Smail, I., Chapman, S. C., Blain, A. W., Ivison, R. J., & Keel, W. C. 2004, ApJ, 617, 64

Symeonidis, M., et al. 2013, MNRAS, 431, 2317

Tacconi, L. J., et al. 2010, Nat, 463, 781

Takeuchi, T. T., Buat, V., & Burgarella, D. 2005, A&A, 440, L17

Tresse, L., Rola, C., Hammer, F., Stasińska, G., Le Fevre, O., Lilly, S. J., & Crampton, D. 1996, MNRAS, 281, 847 Veilleux, S., Kim, D.-C., Sanders, D. B., Mazzarella, J. M., & Soifer, B. T. 1995, ApJS, 98, 171

Whitaker, K. E., et al. 2011, ApJ, 735, 86

Wisnioski, E., Glazebrook, K., Blake, C., Poole, G. B., Green, A. W., Wyder, T., & Martin, C. 2012, MNRAS, 422, 3339

Wisnioski, E., et al. 2011, MNRAS, 417, 2601

Wright, E. L., et al. 2010, AJ, 140, 1868

Wuyts, S., et al. 2007, ApJ, 655, 51

Zurita, A., Rozas, M., & Beckman, J. E. 2000, A&A, 363, 9